DTU Library

Observations of interplanetary dust by the Juno magnetometer investigation

Benn, Mathias; Jørgensen, John Leif; Denver, Troelz; Brauer, Peter; Jørgensen, Peter Siegbjørn; Andersen, A. C. ; Connerney, J. E. P.; Oliversen, R. J.; Bolton, S. J.; Levin, S. M.

Key Points:
- Star cameras included on the Juno spacecraft payload as part of the magnetometer investigation identified and tracked small objects in close proximity to the spacecraft
- The tracked objects are identified as submillimeter particles excavated from the spacecraft, liberated by impact of interplanetary dust particles on the spacecraft solar arrays
- The number and timing of such impacts provide useful information about the distribution, sources, and sinks of interplanetary dust in the solar system.

Observations of interplanetary dust by the Juno magnetometer investigation

M. Benn[1] [ID], J. L. Jorgensen[1] [ID], T. Denver[1] [ID], P. Brauer[1], P. S. Jorgensen[1] [ID], A. C. Andersen[2] [ID], J. E. P. Connerney[3,4] [ID], R. Oliversen[4], S. J. Bolton[5] [ID], and S. Levin[6] [ID]

[1]DTU-Space, Technical University of Denmark, Kongens Lyngby, Denmark, [2]Dark Cosmology Centre, Niels Bohr Institute, University of Copenhagen, Copenhagen, Denmark, [3]Space Research Corporation, Annapolis, Maryland, USA, [4]NASA Goddard Space Flight Center, Greenbelt, Maryland, USA, [5]Southwest Research Institute, San Antonio, Texas, USA, [6]Jet Propulsion Laboratory, Pasadena, California, USA

Abstract One of the Juno magnetometer investigation's star cameras was configured to search for unidentified objects during Juno's transit en route to Jupiter. This camera detects and registers luminous objects to magnitude 8. Objects persisting in more than five consecutive images and moving with an apparent angular rate of between 2 and 18,000 arcsec/s were recorded. Among the objects detected were a small group of objects tracked briefly in close proximity to the spacecraft. The trajectory of these objects demonstrates that they originated on the Juno spacecraft, evidently excavated by micrometeoroid impacts on the solar arrays. The majority of detections occurred just prior to and shortly after Juno's transit of the asteroid belt. This rather novel detection technique utilizes the Juno spacecraft's prodigious 60 m^2 of solar array as a dust detector and provides valuable information on the distribution and motion of interplanetary (>μm sized) dust.

Plain Language Summary The Juno magnetometer investigation uses star cameras co-located with the magnetic sensors at the outer end of one of Juno's solar arrays. These cameras compare images with an onboard star catalog to determine the orientation of the sensors in inertial space. They also serendipitously recorded multiple images of small particles excavated from the spacecraft by high-velocity dust impacts. We trace their trajectories back in time to demonstrate that they evolved from the spacecraft. This allows us to use the vast collecting area of Juno's solar arrays (60 m^2) as a novel dust detector, sensitive to particles with a mass range never before measured in situ.

1. Introduction and Methods

The Magnetometer investigation onboard the Juno spacecraft [*Connerney et al.*, 2017] is optimized to map the magnetic field of Jupiter with 100 parts per million absolute vector accuracy. The fluxgate magnetometer sensors are located at ~10 and ~12 m from the body of the spacecraft on a dedicated 4 m magnetometer boom at the end of one of the Juno spacecraft's three solar panel wings. Each fluxgate magnetometer resides on a magnetometer optical bench that accommodates a pair of nonmagnetic star cameras that together provide accurate attitude estimates at the location of each sensor. These cameras (Camera Head Units or CHUs) are part of the Advanced Stellar Compass (ASC) attitude determination system, without which the vector accuracy of the magnetometer investigation would be limited by the mechanical deformations of the solar array and magnetometer boom throughout variations in environmental conditions. The four CHUs that serve the attitude determination function are miniature low-light cameras, delivering images of the star field to a redundant central data processing unit located in the main body of the spacecraft. These images record luminous objects in the wavelength band of 380 nm–760 nm and contain stars and other luminous objects in the intensity range from visual magnitude $V = -2$ down to $V = \sim7.4$.

Juno is a spinning spacecraft, rotating about the spacecraft payload $+z$ axis (nearly aligned with the fixed parabolic telecom antenna) at a rotation rate of 1 or 2 rotations per minute during cruise. The ASC CHUs image the celestial sphere with a 13° by 18° field of view (FOV) and are oriented with a separation of 13° between the camera boresight and the spacecraft ($-z$) spin axis [*Connerney et al.*, 2017]. Juno is a solar-powered spacecraft, normally oriented with the $+z$ axis toward the Earth (for telecom) and the Sun (for power), so during a rotation each CHU images a washer-shaped region of the celestial sphere in the

antisunward direction. The CHUs are boresighted near the spin axis to minimize image smear during an exposure (0.25 s).

The ASC has the difficult task of identifying stars in the camera field of view (FOV) and associating the pattern of valid star images with a unique such pattern of stars stored in the onboard star catalog, thereby determining attitude of the CHU. Therefore, it is important to identify and discard spurious responses, whether due to sensor response to penetrating radiation or identification of objects not among those in the star catalog. The severe radiation exposure experienced during Juno's orbit is mitigated by shielding mass provided around and within the ASC camera heads. However, very energetic particles (≥10 MeV) will penetrate the CHU [*Becker et al.*, 2017] and may impact the active region of the CCD sensor. The charge deposition from such particles results in a CCD response that must be identified and removed by the ASC before nominal star identification can be performed. This function is performed by a set of morphological filters, ultimately returning a cleansed star image to the ensuing attitude determination algorithms. The attitude determination process includes a validation step, whereby the luminous objects identified in a given image are matched to those in the onboard star catalog. Any luminous object not included in the catalogue is registered as a Non-Stellar-Object (NSO), along with the object's apparent inertial position and intensity.

Objects detected and identified as NSOs can be real stars that are not among those in the catalogue, other spacecraft, planetesimals, asteroids, moons, planets, or, if close enough, dust particles. We use observation of the rate of change of the apparent position between observations to discriminate among these objects: stars and distant solar system bodies will necessarily move with an apparent speed of arcsec/s or less, whereas objects closer to the spacecraft will exhibit a higher angular rate. Radiation effects not removed by the morphological filters will only persist in one image. Therefore, the detection strategy designed to track proximate objects is configured to isolate only those objects with an apparent angular rate between 2 arcsec/s and 18,000 arcsec/s. In addition, an object must be recorded in more than five sequential images, in any 120 s period, to be admitted to the group.

A fast-moving object traversing the star field may naturally pass close to stars in the star catalogue. When an object is detected within 800 arcsec of a catalog star, the detection is not included in the recorded sequence, but the object's history remains, so when the object eventually moves beyond the 800 arcsec keep-out-zone, tracking continues [*Benn*, 2011]. This set of filters ensures that only faster-moving objects are recorded. Despite the aforementioned sorting, more than 0.5 million such NSO observations were returned during the cruise from Earth to Jupiter (NSO tracking was enabled for 3.5 of the 5 year cruise period). We report here on a very small subset of these objects for which precise trajectories have been computed. Previous spacecraft (e.g., STEREO A and B at 1 AU) have serendipitously imaged impact ejecta [*St. Cyr et al.*, 2009; *Davies et al.*, 2012] in long-duration exposures; Juno's CHUs are the first to autonomously detect and characterize ejecta mass and velocity via a series of short-duration exposures.

2. Observations

A small number of objects exhibiting very high angular velocities were detected. Observation by a single camera does not allow a determination of the distance to an unknown object. The distance to an object is, however, constrained by the laws of motion for a solar system body. As these objects also exhibit a continuous decrease in intensity of reflected light over the brief tracking period, they must be proximate objects moving away from the spacecraft, rather than large and more distant fast-moving bodies passing through our solar system (hyperbolic trajectories). Reasonable assumptions on the size and albedo of this class of object would result in size estimates in the few meter range, provided they belong to the main asteroid belt [e.g., *Izidoro et al.*, 2016, and references therein]. Several of the objects were found to have trajectories very close to each other, rendering as improbable main belt asteroids as targets.

A more detailed analysis revealed that these objects also exhibit a pattern of motion that deviated from that expected of a distant object (straight line in inertial space). During the brief span of time these objects were tracked (~5 to ~20 s) their motion followed a smooth curved trajectory. This pattern of motion is only consistent with force-free objects moving along with Juno and at nearly the same speed as the spacecraft, i.e., so close, that the camera, mounted 10 m from the center of the spacecraft, observes the object with measurable parallax during a spacecraft rotation.
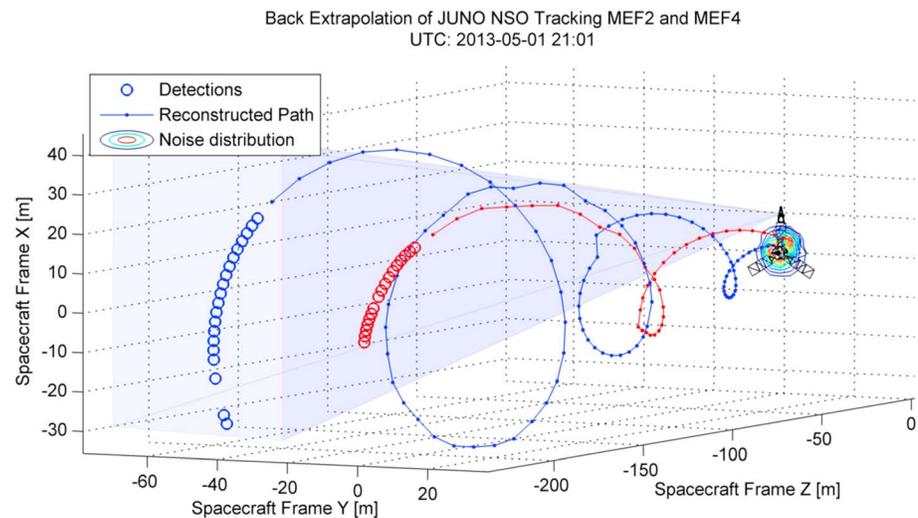
Figure 1. Backward extrapolation of two NSO trajectories observed during a main engine flush (MEF) event. The open circles represent object detections for which object position and intensity information are available, and the closed circles are extrapolated positions extending back to the spacecraft plane. The uneven behavior of the reconstructed path is due to the change in attitude (disturbance) associated with the MEF events.

Juno had already been in cruise for more than 1 year at the start of the NSO observation campaign immediately following Earth flyby. By this time Juno had already experienced numerous trajectory correction maneuvers, including a main engine burn of ~300 s duration, as well as relatively high surface temperatures at perihelion inside the orbit of Venus. Objects traveling along with the spacecraft or evaporated from spacecraft surfaces (often observed by star trackers in low Earth orbit just after launch) are thus implausible. Liberation of objects large enough (of order millimeter) to provide the observed intensity of reflected sunlight requires substantial energy, which leaves but two candidates as a source of the objects: particles liberated by propulsive maneuvers or particles excavated by impacts from dust particles moving at high relative velocity. Interplanetary dust particles (IDPs) in near-circular Keplerian orbits about the Sun may be expected to have ~15 to ~5 km/s velocities relative to Juno, providing more than enough energy to excavate detectable target material.

We distinguish between these two types of objects by careful analysis of the variation in intensity of reflected light from the object and analysis of the object's trajectory. The apparent position of the object as a function of time (during the spacecraft rotation) can be used to determine the distance and radial velocity components of the object relative to the observer (camera). Thus, the trajectory of the object in the spacecraft reference frame can be determined. Traced back in time, from where it first enters the camera FOV, the object's point of origin can be determined as the x and y coordinates of the object as it is traced to $z = 0$ in the spacecraft frame. The longer an object can be tracked within the FOV of the camera, the more precise the determination of the object's trajectory and accordingly the more accurately the point of origin can be determined.

We have tracked particles resulting from propulsive maneuver procedures, evidently liberated during a procedure described as a main engine flush (MEF). Examples of two such objects are shown in Figure 1. These objects were identified by our tracking and filtering algorithms, but further analysis showed that these objects originated near the center of the spacecraft and examination of the mission log revealed that these objects were observed seconds to minutes following a main engine activity, typically a MEF.

These objects offer an excellent test of tracing methods and trajectory propagation algorithms, but being entirely of spacecraft operations origin, they are of little interest otherwise. To eliminate such particles, all observations within 30 min of a scheduled main engine activity have been excluded from our analyses. This span of time was selected because the actual time of execution of main engine procedures may vary from the schedule by a few minutes, and it takes some time for the spacecraft to settle completely after such a maneuver (possibly dislodging a particle during such movement). Spacecraft noninertial behavior is
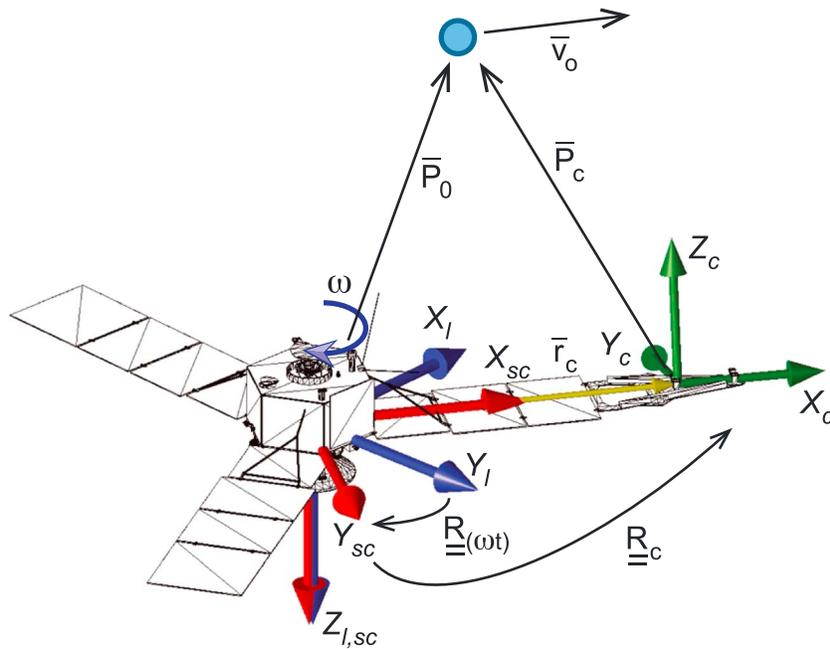
Figure 2. Definitions for the Juno spacecraft reference frame, camera reference frame, and the velocity and position vectors of the detected object. Z-SC adjusted to camera center.

observed to persist for minutes after execution of a typical engine procedure, as is clearly visible in the example shown in Figure 1.

3. Analysis

The trajectory of a distant solar system object in an inertial frame may be approximated for short observation times by a straight line. The parallax resulting from the rotation (radius vector of 10 m) of the ASC camera about the spacecraft center is 1 arcsec (a fiducial reference; camera accuracy on the spinning platform is ~10 arcsec) for an object at a distance of 4125 km. All objects discussed in this analysis exhibit substantially larger parallaxes; i.e., they are all substantially closer to the spacecraft, typically of order 100 m distant.

The geometry for the observations is depicted in Figure 2. The spacecraft coordinate frame (X_{SC}, Y_{SC}, and Z_{SC}) rotates relative to an inertial frame (X_I, Y_I, and Z_I). Because we only consider relative motions over a short time span, the transform from inertial to rotating spacecraft frame may be described by a pure rotation $\underline{R}(\omega t)$, which is continuously provided by the ASC star trackers at a cadence of 1 measurement per 7 s. During cruise, the Juno spacecraft was programed to rotate with a period of 1 rotation every 30 or 60 s. The ASC camera configured to acquire NSO observations (CHU-D) is offset by the vector r_C and rotated by $\underline{R}_C$ from the spacecraft frame.

An object moving with a relative velocity v_O and observed at P_0 at time $t = 0$ in inertial frame will be observed in the camera frame at $P_C(t)$:

$$P_C(t) = \underline{R}_C \left[\underline{R}(\omega t)(P_0 + v_O t) \right] - r_C \tag{1}$$

The camera observes the apparent position unity vector N_C as long as the object remains in the camera field of view:

$$N_C = P_C(t) / |P_C(t)| \tag{2}$$

The nonlinear equations outlined above may be inverted to obtain a solution. However, since a minimization for the best model solution with the given measurement noise is sought, the forward iterative scheme described below was used:
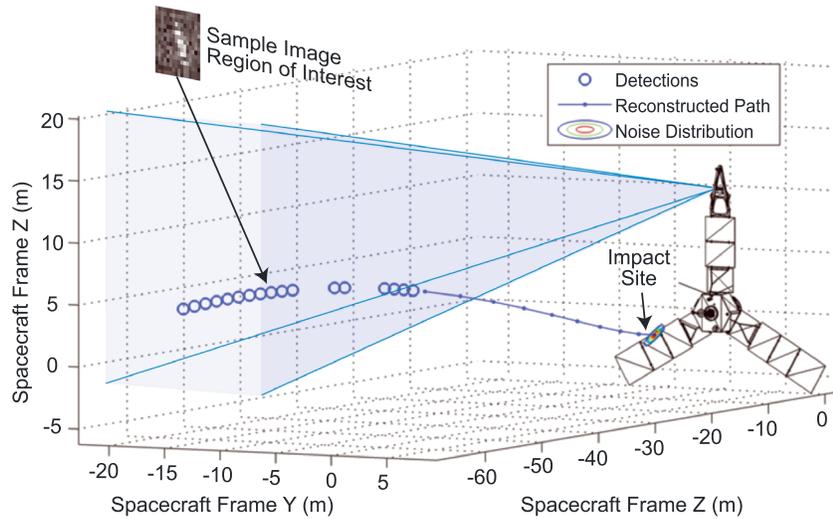
Figure 3. Extrapolation of a NSO trajectory (as in Figure 1) backward in time for an object originating on one of Juno's solar arrays. Error analysis (see text) isolates the object's point of origin to (dark side) one of Juno's three solar panels. Each open circle represents a NSO detection. For each such detection, a region of interest image centered on the object's RA and DEC is stored; one of the 17 such images available for this object is shown.

1. A position is assigned for the first observation of the object and the object's velocity in the inertial frame.
2. Calculate the object's measured unit vector M_C in the camera frame and get the time of observation of the object.
3. Apply equation (1) to these initial estimates, using the known values for $\underline{\underline{R}}_C$, $\underline{R}(\omega t)$, r_C, and the time t of the observation.
4. Find N_C using equation (2).
5. Repeat steps 3 through 5 for all tracking observations.
6. Calculate the formal error according to $e = |M_C - N_C|$.
7. Minimize e iteratively.

The solution found in this manner is well determined since the measurement noise is small compared to the observed parallax. The final step in the procedure is to propagate the object motion solution back in time until the z component of the object's position approaches zero, i.e., to the plane of the Juno solar panels. To quantify the accuracy of the solution, we added random noise (80 arcsec) to each observation, generating a family of slightly different solutions. The result is a family of solutions clustered around the best fit solution as seen in Figures 1 and 3.

4. Results

The best fit model solutions for this group of objects are listed in Table 1. This table displays the velocity and position of the objects at first detection, along with the object's apparent magnitude. All assumptions made in the above analysis regarding the relative motion of the objects are found to be satisfied. Using the

Table 1. Trajectory Solutions for Objects Tracked by the ASC Camera D

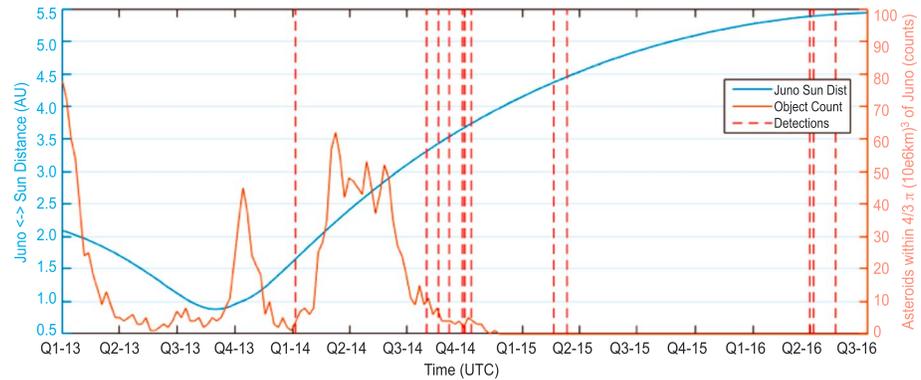| Track UTC (DD-MM-YYYY)	App. Mag. To $t = 0$	Number of Images	$|V_0|$ (m/s)	Traveled Distance From X-Y Plane to $t = 0$ (m)	X-Y Plane Crossing (x,y) (m)		Backward Extrapolation Time (s)
5-1-2014	3.3	10	0.489	22.5	−4.84	−3.35	−43.2
1-8-2014	3.5	6	0.229	16.8	2.76	−1.55	−78.2
1-10-2014	4.4	12	0.843	26.8	8.24	3.39	−37.7
11-10-2014	4.4	8	0.142	20.1	5.79	0.22	−129.35
12-3-2015	5.7	17	4.805	43.8	−2.09	−5.84	−9.3

Figure 4. Objects in this subgroup detected by Juno as a function of time compared with the volume density of asteroids along Juno's flight path [data sources: *Acton*, 1996; *Bowell*, 2017] and Juno's radial distance (AU) from the Sun (blue).

spacecraft distance to the Sun r_{Sun}, the calculated observed distance r_{Obj} and apparent visual magnitude V, and noting that all observations are made with a phase angle near zero, the object diameter D multiplied by the square root of the visual albedo ρ_V can be estimated as

$$D \cdot \rho_V = 1329 \cdot 10^{-V/5} \cdot r_{Sun} \cdot r_{Obj} \qquad (3)$$

An object excavated from the spacecraft may exhibit an albedo ranging between 0.05 and 0.95, with either extreme being very unlikely. Large impact ejecta suffer little melting or chemical change, so we assume a visual albedo equal to that of the target material (e.g., Germanium Kapton tape with albedo 0.07). With this albedo, the first object in Table 1 has a diameter of 0.3 mm, and correspondingly a mass of ~30 μg (density 2 g cm^3). All objects detected by this method exhibit an estimated diameter between 0.1 and 1 mm. An IDP with velocity 5 to 15 km s^{-1} may be expected to excavate a mass of ~120 to 1000 times its own mass [*Morfill et al.*, 1983; *Dohnanyi*, 1969]. Therefore, the incoming dust particle must have been at least in the range of tens of nanograms, delivering an impact energy of 3–10 mJ, depending on the impact velocity. Such particles are more massive than those detected by the dedicated dust detectors flown on Ulysses and Galileo [*Grun et al.*, 1992a, 1992b; *Kruger et al.*, 2015], for example.

An estimate of the efficacy of the detection method can be derived from the detector geometry and a reasonable constraint on the relative velocity of the excavated objects. Particles in Keplerian orbit will exhibit relative velocities of ~15 to 5 km/s. Particles detected in association with spacecraft activities, such as main engine flushes or pressure valve cycling, are confidently tracked at relative velocities up to 5 m/s. Since the impact-excavated objects we detected are moving more slowly, we assume that the velocity characteristic [*Rival and Mandeville*, 1999] of large ejecta particles will not affect detection; i.e., the detection efficacy d_V over velocity range is close to 1. The FOV of the camera covers 1/120 of the night sky. The circular motion of the camera during a complete rotation of the spacecraft yields a reasonable geometric detection efficacy $d_G = 0.1$.

Large ejecta (>200 μm) are bright enough to return sufficient light to the camera to ensure detection from the entire Juno ram side solar array surface area, $A_J = 60$ m^2. Smaller objects must cross the camera FOV at closer distances in order to be detected the requisite minimum of 5 times. For example, a 50 μ object would only be detectable to ~20 m distance. An overall size efficacy $d_E = 0.7$ is assumed, for the particles we do observe, based on the size distribution of the particles we detect, and an assumed albedo 0.07.

These considerations lead to an estimated instrument detectivity $d_I = d_E \cdot d_G \cdot d_V \cong 0.07$. We now provide an estimate of the number density of IDPs that we are sensitive to using the group (of 6) detected during a 90 day interval (quarter 4, 2014), while Juno was ~3.5 AU from the Sun. With 60 m^2 of target area at an angle of ~45° to circularized IPD, this corresponds to a detection rate of $6/(60 \times \cos(45°) \times 90 \times 86400) = 1.8 \times 10^{-8}$ detections m^{-2} s^{-1}.

The spacecraft velocity relative to circularized IPD particles at this time was ~14 km s^{-1}, yielding a number density of particles detected:

$$1.8 \times 10^{-8} / 1.4 \times 10^4 = 1.29 \times 10^{-12} \text{ m}^{-3}$$

Accounting for the estimated detection efficacy of ~0.07, we arrive at the number density of IDPs (in the size range we can detect via their ejecta) of 1.8×10^{-11} m^{-3}. This number density is comparable to *Grun et al.*'s [1997] IDP number density for ~1 μg particles and a factor 10 greater than the estimated number density of "asteroidal" group IDPs for all IDP masses <10 μg. Interplanetary dust particles some tens of microns in size at 5–15 km s^{-1} velocities can easily supply the large ejecta we observe, particularly if most of the ejecta mass evolves in the form of a small number of spall products traveling at relatively low velocities [*Rival and Mandeville*, 1999; *Vetter and Mandeville*, 1974].

5. Conclusions

We have demonstrated the dust detection capability of Juno's ASC instrumentation, using Juno's solar arrays as a 60 m^2 target for dust impacts. The CHUs detect and register small luminous objects, providing in some cases enough information to accurately determine the trajectory of objects proximate to the spacecraft. These objects are excavated by high-velocity dust particle impacts on the solar arrays. Impacts were only detected prior to entry into the main asteroid belt and subsequent to Juno's emergence from the main asteroid belt (Figure 4). No impacts were observed during Juno's transit of the main asteroid belt. This implies that the dust grains we observe with this method are in Keplerian orbit about the Sun and exist in orbits that are less effectively swept up by collisions with asteroids within the main belt. They are of the "asteroidal" group of IDPs, particles too massive (>10^{-10} g) to be influenced by radiation pressure ($\beta = 0$) and orbiting the Sun in low eccentricity, low inclination (<30°) orbits [*Grun et al.*, 1997].

The distribution of impacts observed during Juno's traverse of the inner solar system may constrain the efficacy of the Poynting-Robertson effect [*Poynting*, 1903; *Robertson*, 1937] in clearing dust from a stellar nebula. The Poynting-Robertson effect causes dust grains small enough to be affected by this drag and too large to be blown away from the star by radiation pressure (typically particles ~1 μ to 1 mm in diameter), to spiral slowly into the star. The role of the Poynting-Robertson effect is an important part of our understanding of early solar system evolution. Juno observations also provide valuable information on a population of IDPs beyond that sampled by small-aperture dedicated dust detectors, information only indirectly provided (at 1 AU) by studies of micrometeorites transiting the lower stratosphere or recovered in Antarctica [*Mackinnon and Rietmeijer*, 1987; *Maurette*, 2009].

In this work we concentrated on a small subset of the objects for which an extended tracking history is available. We demonstrate that the Juno observations are relevant to studies of the micrometeoroid environment in our solar system and that the Juno investigation provides valuable information regarding a population of particles that has thus far eluded systematic detection and characterization. We will, in subsequent work, extend our study to the vast majority of detected objects for which precise trajectories cannot be determined, comparing these Juno observations with those provided by the dust experiments on the Ulysses and Galileo spacecraft and dust samples returned by the Stardust spacecraft [*Westphal et al.*, 2014]. We expect to characterize the number density of the asteroidal population of IDPs from Earth orbit to Jupiter, providing valuable information on the sources and loss processes of asteroidal group IDPs.

References

Acton, C. H. (1996), Ancillary data services of NASA's Navigation and Ancillary Information Facility, *Planetary and Space Science*, 44(1), 65–70.

Becker, H. N., et al. (2017) Observations of high energy electrons in Jupiter's innermost radiation belts and polar regions by the Juno radiation monitoring investigation: Perijoves 1 and 3, *Geophys. Res. Lett.*, 44, doi:10.1002/2017GL073091, in press.

Benn, M. (2011) Vision based navigation sensors for spacecraft rendezvous and docking, Ph.D. thesis, Technical University of Denmark (DTU), Kgs. Lyngby, Denmark.

Bowell, E. (2017) The asteroid orbital elements database, Lowell Observatory http://asteroid.lowell.edu/ Objects:726349.

Connerney, J. E. P., et al. (2017), The Juno magnetic field investigation, *Space Sci. Rev.*, doi:10.1007/s11214-017-0334-z.

Davies, C. J., et al. (2012), The distribution of interplanetary dust between 0.96 and 1.04 AU as inferred from impacts on the STEREO spacecraft observed by the heliospheric imagers, *Mon. Not. R. Astron. Soc.*, 420, 1355–1366.

Dohnanyi, J. S. (1969), Collisional model of asteroids and their debris, *J. Geophys. Res.*, 74(10), 2531–2554, doi:10.1029/JB074i010p02531.

Grun, E., H. Fechtig, M. S. Hanner, J. Kissel, B. A. Linblad, D. Linkert, D. Maas, G. E. Morfill, and H. A. Zook (1992a), The Galileo dust detector, *Space Sci. Rev.*, 60, 317–340.

Grun, E., H. Fechtig, J. Kissel, D. Linkert, D. Maas, J. A. M. McDonnell, G. E. Morfill, G. Schwehm, H. A. Zook, and R. H. Giese (1992b), The Ulysses dust experiment, *Astron. and Astrophys. Supplement*, 92, 411–423.

Grun, E., et al. (1997), South-north and radial traverses through the interplanetary dust cloud, *Icarus*, 129, 270–288.

Izidoro, A., S. N. Raymond, A. Pierens, A. Morbidelli, O. C. Winter, and D. Nesvorny (2016), The asteroid belt as a relic from a chaotic early solar system, *ApJ*, *833*, 1–18.

Kruger, H., P. Strub, E. Grun, and V. J. Sterken (2015), 16 years of Ulysses dust measurements in the solar system: I. Mass distribution and gas-to-dust mass ratio, *Astrophys. J.*, *812*, 139.

Mackinnon, I. D. R., and F. J. M. Rietmeijer (1987), Mineralogy of chondritic interplanetary dust particles, *Rev. Geophys.*, *25*, 1527–1553, doi:10.1029/RG025i007p01527.

Maurette, M. (2009), Hydrous-carbonaceous meteoroids in the Hadean Aeon, *ASPC*, *414*, 137–147.

Morfill, G. E., H. Fethig, E. Grun, and C. K. Goertz (1983), Some consequences of meteoroid impact on Saturn's rings, *Icarus*, *55*, 439–447.

Poynting, J. H. (1903), Radiation in the solar system: Its effect on temperature and its pressure on small bodies, *MNRAS*, *64*, 1–5.

Rival, M., and J. C. Mandeville (1999), Modeling of ejecta produced upon hypervelocity impacts, *Space Debris*, *1*, 45–57.

Robertson, H. P. (1937), Dynamical effects of radiation in the solar system, *MNRAS*, *97*, 423–438.

St. Cyr, O. C., et al. (2009), STEREO SECCHI and S/WAVES observations of spacecraft debris caused by micron-size interplanetary dust impacts, *Solar Phys.*, *256*, 475–488.

Vetter, J. F., and J. C. Mandeville (1974), Microcraters formed in glass by projectiles of various densities, *J. Geophys. Res.*, *79*(23), 3247–3256, doi:10.1029/JB079i023p03247.

Westphal, A. J., et al. (2014), Evidence for interstellar origin of seven dust particles collected by the stardust spacecraft, *Science*, *345*, 786–791.